Near-field acoustic streaming jet

B. Moudjed,[1] V. Botton,[1] D. Henry,[1] S. Millet,[1] J. P. Garandet,[2] and H. Ben Hadid[1]

[1]*Laboratoire de Mécanique des Fluides et d'Acoustique, CNRS/Université de Lyon, École Centrale de Lyon/Université Lyon 1/INSA de Lyon,*
ECL, 36 avenue Guy de Collongue, 69134 Ecully Cedex, France

[2]*CEA, Laboratoire d'Instrumentation et d'Expérimentation en Mécanique des Fluides et Thermohydraulique,*
DEN/DANS/DM2S/STMF/LIEFT, CEA-Saclay, F-91191 Gif-sur-Yvette Cedex, France

A numerical and experimental investigation of the acoustic streaming flow in the near field of a circular plane ultrasonic transducer in water is performed. The experimental domain is a parallelepipedic cavity delimited by absorbing walls to avoid acoustic reflection, with a top free surface. The flow velocities are measured by particle image velocimetry, leading to well-resolved velocity profiles. The theoretical model is based on a linear acoustic propagation model, which correctly reproduces the acoustic field mapped experimentally using a hydrophone, and an acoustic force term introduced in the Navier-Stokes equations under the plane-wave assumption. Despite the complexity of the acoustic field in the near field, in particular in the vicinity of the acoustic source, a good agreement between the experimental measurements and the numerical results for the velocity field is obtained, validating our numerical approach and justifying the planar wave assumption in conditions where it is *a priori* far from obvious. The flow structure is found to be correlated with the acoustic field shape. Indeed, the longitudinal profiles of the velocity present a wavering linked to the variations in acoustic intensity along the beam axis and transverse profiles exhibit a complex shape strongly influenced by the transverse variations of the acoustic intensity in the beam. Finally, the velocity in the jet is found to increase as the square root of the acoustic force times the distance from the origin of the jet over a major part of the cavity, after a strong short initial increase, where the velocity scales with the square of the distance from the upstream wall.

I. INTRODUCTION

The ability of acoustic fields to drive steady flows in fluids has been known for decades [1] and is usually referred to as acoustic streaming. This phenomenon is, willingly or not, present in a number of applications ranging from ultrasound-based velocimetry [2,3] to medical applications [4,5] and from heat and mass transfer [6–10] to sonochemistry [11]. It can also be used to move particles [12] or droplets [13] or to generate jets in small and even microsize domains [14]. It can be seen as a coupling between acoustic propagation and fluid motion [15]. This coupling is often accounted for by an additional force term in the Navier-Stokes equations for a viscous incompressible flow. For an acoustic plane wave propagating along the x direction, this force [16,17] can be expressed, at every location X, as

$$\vec{f}_{\text{ac}}(X) = \frac{2\alpha}{c} I_{\text{ac}}(X)\vec{x}, \qquad (1)$$

where I_{ac} is the acoustic intensity, α is the acoustic pressure wave attenuation coefficient ($\alpha = 0.1$ m^{-1} for water at 20 °C and an acoustic frequency $f = 2$ MHz), and c is the sound celerity ($c = 1480$ m s^{-1} for water at 20 °C). The acoustic field, however, is known to often involve diffraction effects, as shown in our recent experimental investigation in the acoustic far field [17]. The flow structure was found to be strongly correlated to the shape of the acoustic beam, so a conclusion was that accounting for diffraction is a key ingredient in the modeling of acoustic streaming. However, as the near field exhibits complicated patterns for the space variations of I_{ac}, the question about the validity of the plane-wave assumption used to obtain Eq. (1) can be raised.

A few years ago, Kamakura *et al.* [18] performed an experimental and theoretical study of acoustic streaming in the near field of a circular plane transducer. Their theoretical approach relies on a physically intricate nonlinear propagation model including diffraction, attenuation, and nonlinear effects to compute the acoustic streaming force field. They solve the Khokhlov-Zabolotskaya-Kuznetsov (KZK) equation [19,20] with appropriate boundary conditions for the acoustic pressure. From the obtained acoustic pressure field, they deduce the force term to be included in the Navier-Stokes equations, which they solve using a stream-function vorticity method. A limit of this approach is that solving the KZK equation for the propagation problem is very time-consuming since this transient nonlinear equation must be solved on every point of the mesh used for the Navier-Stokes solver, though the significance of the acoustic nonlinearity influence on the generated velocity field remains questionable. In the same paper, Kamakura *et al.* [18] investigate the acoustic streaming velocity field using the laser Doppler anemometry (LDA) technique, which allows a local measurement of the velocity. They obtain detailed transverse velocity profiles but have a poor spatial resolution in their longitudinal velocity profiles, with only six data points for the 27-cm-long fluid domain. The comparison between the numerical and experimental transverse velocity profiles supports the reliability of their numerical model. However, the numerically obtained longitudinal velocity profiles exhibit an undulating shape which cannot be confirmed experimentally due to the lack of spatial resolution. Our contention is that such a shape can probably be correlated to the complex longitudinal profile of the acoustic beam in the near field. Such correlation between velocity and acoustic intensity is only discussed in Kamakura *et al.* [18] for transverse profiles taken close to the Fresnel length.

They underscore the fact that the velocity profile shape only transiently looks similar to the acoustic intensity profile shape, i.e., featuring one central peak and two secondary local maxima; on the contrary, the steady-state velocity profile features only one, smooth, maximum on the centerline. For the other velocity profiles taken closer to the source, unfortunately, no explicit velocity to acoustic intensity comparison is given.

Note, finally, that Lighthill [15] discussed the different types of streaming generated by an attenuated acoustic beam and the resulting flow structures. More recently, Bradley [21] studied analytically the acoustic streaming field structure taking into account the displacement of the acoustic radiator: The expressions obtained include new terms, but these terms are mainly important in gases. These authors, however, did not consider the specific shape of the acoustic field in the near field due to Fresnel diffraction and its influence on the flow structure.

In the present paper the geometry is close to that of Kamakura *et al.* [18], although the diameter and the frequency of the source differ. The former study [18] indeed considered a higher frequency f, but a smaller source diameter d_s, so the near-field size, i.e., the Fresnel length $L_f = d_s^2/(4\lambda)$ (where λ is the acoustic wavelength), is similar in both studies. An objective of our study is to experimentally validate the force model given by Eq. (1) in the near-field region where the legitimacy of the plane-wave assumption is questionable. For that we rely on space-resolved velocity profiles obtained by use of the particle image velocimetry (PIV) technique. Another objective is to show that a numerical model based on linear acoustic propagation is able to accurately simulate this type of flow in the investigated parameters range. We also want to confirm that steady-state transverse velocity profiles can show strong similarities with intensity profiles, for instance, concerning the number of local maxima. A final objective is to provide scaling laws for the velocity on the acoustic beam axis.

II. EXPERIMENTAL SETUP

The experiments are performed within an aquarium filled with water. The sound source is a 2-MHz ultrasonic circular plane transducer from Imasonic, with a diameter of 29 mm.

As depicted in Fig. 1, the domain of investigation is a rectangular cavity of inner dimensions $265 \times 180 \times 160$ mm^3 (length $\times$ width $\times$ height) with a top free surface. It is delimited by two 10-mm-thick Apflex F28 absorbing walls, hatched on the figure, from Precision Acoustic. The end wall is placed at $x_L = 275$ mm from the transducer, i.e., at the end of the acoustic near field, in order to prevent standing waves to form in the investigated domain. The other wall, referred to as the intermediate tile and placed close to the transducer, has been drilled with a 63-mm hole. The diameter of the hole has been chosen as about twice the transducer diameter in order to avoid modifying the acoustic pressure field. The hole was covered with a thermoretractable plastic film (plastic film that retracts when heated, allowing a film which is tight and flat) to let the sound enter into the investigation area but, at the same time, to provide a rigid wall condition for the generated flow. The distance between the transducer surface and the plastic film is $x_0 = 10$ mm. This setup has already been described in our previous experimental paper [17]; it is also presented in more detail by Moudjed [22].

A needle hydrophone from Precision Acoustics, held on a three-dimensional (3D) motorized system, is used to map the acoustic field. A Lavision PIV system is used to measure velocity fields. Image acquisition is made with a 12-bit PCO Sensicam charge-coupled device camera with a resolution of 1280×1024 pixels. In our measurements, we use a double frame mode with a frequency of 4 Hz; 6000 double frames are acquired as soon as the transducer is switched on, so acquisition lasts about 25 min. The time between the frames of each image pair is chosen to be 120, 90, and 50 ms for transducer electric powers of respectively 2, 4, and 8 W, in order to optimize the apparent displacement of the seeding particles. The deionized water used was seeded with 5-μm polyamid seeding particles (PSP) of density 1030 kg m^{-3} from Dantec. The water temperature was measured to be 23 °C. Care should be taken to adjust the position and the thickness of the laser sheet since velocity gradients are strong. A 3D motorized displacement ensures the precise positioning and a homemade optical system is used to generate a laser sheet of less than 1 mm in thickness.

PIV measurements were made in two 20-cm-long and 16-cm-wide areas of the xy horizontal middle plane with an
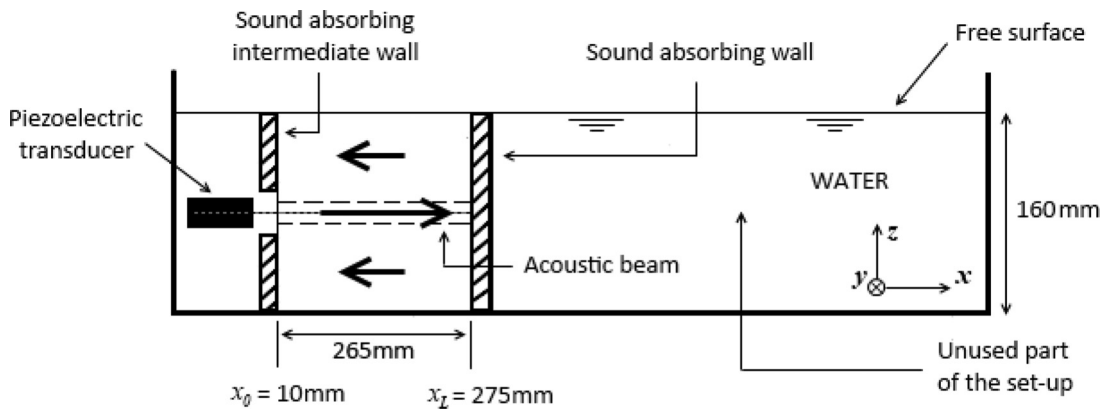

FIG. 1. Experimental setup, view from the side. The origin of the Cartesian frame is set at the middle of the transducer plane surface: x axis coincides with the propagation direction, and the y and z axes are, respectively, horizontal and vertical. The overall length of the aquarium is 900 mm.

overlap region to ensure a sufficient spatial resolution while observing the whole region of interest. The first zone extends from $x = 10$ mm, i.e., from the intermediate sound-absorbing wall, to $x = 205$ mm and the second zone extends from $x = 80$ to $x = 275$ mm, i.e., to the downstream sound-absorbing wall.

III. NUMERICAL MODEL

To simulate the flow, we consider a rectangular cavity with dimensions $265 \times 180 \times 160$ mm^3 (length $\times$ width $\times$ depth) filled with water. The top free surface is assumed to be a plane with a free-slip condition for the flow and all the other boundaries are considered as rigid with a no-slip condition. Laminar, 3D, incompressible computations are performed with the commercial software STARCCM+, which solves the Navier-Stokes equations with an additional acoustic force term:

$$\rho \frac{d\vec{u}}{dt} = -\overrightarrow{\text{grad}}\,p + \vec{f}_{\text{ac}} + \mu\Delta\vec{u}, \qquad (2)$$

where $\vec{u}$ is the flow velocity (m s^{-1}), p is the hydrodynamic pressure (Pa), $\vec{f}_{\text{ac}}$ is the volumetric acoustic force (N m^{-3}) defined by Eq. (1), ρ is the fluid density ($\rho = 1000$ kg m^{-3}),

and μ is the dynamic viscosity ($\mu = 10^{-3}$ Pa s). This equation was derived with a time-scale separation method, which is detailed in a former paper [17].

Cubic cells are used to mesh the fluid domain. A cylindrical zone, where the mesh is refined, is created around the location of the acoustic beam. A mesh convergence study lead us to choose cells with a 0.5-mm side in the central cylindrical zone and with a 2-mm side in the rest of the fluid domain [22]; the total number of cells is then 3.82 million. The acoustic force is computed with MATLAB at each cell center using Eq. (1). The calculation of the acoustic intensity field, which appears in Eq. (1), is based on the Huygens-Fresnel assumption. The plane circular acoustic source is discretized with 200×200 elements. Each element has a surface $\Delta S = \sigma\Delta\sigma\Delta\theta$, where σ and θ are the polar coordinates (in the yz plane) of the element center, and is considered a secondary source emitting a spherical wave. The resulting acoustic pressure field is calculated at any location (x, y, z) in the fluid domain by adding each secondary source contribution (Rayleigh's integral). It is a complex quantity from which the phase of the wave and, assuming a plane-wave assumption, the acoustic intensity can be deduced. This acoustic intensity is thus expressed as

$$I_{\text{ac}} = \frac{I_{\text{ac max}}}{4\lambda^2}\left|\sum_{n=1}^{N}\sum_{m=1}^{M}\frac{e^{-i\frac{2\pi}{\lambda}\sqrt{x^2+y^2+z^2+\sigma_n^2-2\sigma_n y\cos(\theta_m)-2\sigma_n z\sin(\theta_m)}}}{\sqrt{x^2+y^2+z^2+\sigma_n^2-2\sigma_n y\cos(\theta_m)-2\sigma_n z\sin(\theta_m)}}\sigma_n\Delta\sigma\Delta\theta\right|^2, \qquad (3)$$

where $I_{\text{ac max}}$ is the maximal acoustic intensity, which is reached at the different peaks on the beam axis, the last peak being located at the Fresnel length [23] [see also Fig. 4(b)]. The source diameter, d_s, is implicitly present in Eq. (3) since it defines the maximum value of σ_n. The acoustic intensity field given by Eq. (3) can be adjusted to the I_{ac} measurements by means of a least-mean-squares method, with two adjustable parameters, $I_{\text{ac max}}$ and d_s. Though we consider the hydrophone measurements to be reliable in a relative sense to obtain the acoustic pressure spatial variations in an experimental run, they are, however, very imprecise concerning acoustic pressure values in an absolute sense; the confidence interval given by Precision Acoustics, the supplier of this gauge, is indeed $\pm 13\%$ on the acoustic pressure, i.e., $\pm 26\%$ on the acoustic intensity. Moreover, the hydrophone measurements cannot be done at the same time as the velocity measurements in our experimental setup. Another issue is that the determination of $I_{\text{ac max}}$ from the applied electric power P is also not possible as neither the electric losses nor the efficiency of the transducer can be accurately measured in our system. As a consequence, we consider that reliable values of $I_{\text{ac max}}$ cannot be directly deduced from these measurements. We then rather chose to make an adjustment between the longitudinal velocity profiles obtained in the experiments and simulations by tuning the acoustic force level used in the simulations. This allows us to get rid of the uncertainties on the hydrophone measurements, the efficiency and losses of the acoustic source, but also of those on the acoustic attenuation coefficient, already discussed in our former paper [17]. The acoustic force level is characterized by the maximum value of the force, $f_{\text{ac max}}$,

reached, for example, on the beam axis at the Fresnel length. Rough adjustments lead to the values $f_{\text{ac max}} = 0.725$, 1.5, and 2.9 N m^{-3} to be used in our simulations to compare with the experiments at $P = 2$, 4, and 8 W, respectively. Note the good proportionality between the chosen $f_{\text{ac max}}$ values and the applied electric powers.

Note also that an adjustment based on the normalized fields of I_{ac} led to $d_s = 28.5$ mm, a value which is very close to the transducer nominal diameter (namely 29 mm), indicating that the structures of the measured acoustic field and the theoretical I_{ac} field are very close; it is confirmed when comparing normalized transverse acoustic intensity profiles (see Moudjed [22] for more details). With this value of d_s, the Fresnel length is $L_f = d_s^2/(4\lambda) = 274$ mm.

The coupled Navier-Stokes solver uses a second-order upwind implicit finite-volume scheme. A steady solver is used for $f_{\text{ac max}} = 0.725$ and 1.5 N m^{-3}; for $f_{\text{ac max}} = 2.9$ N m^{-3}, a second-order implicit time scheme is used. In this last case, the results presented hereunder correspond to the steady regime reached with this unsteady solver.

A question could be raised about the degree of validity of the plane-wave assumption used to derive the expression (1) of the acoustic force. To get some indications on that point, numerically calculated wave fronts of the acoustic wave are given in Fig. 2. They are plotted at $x = 100$ mm [Fig. 2(a)] and $x = 150$ mm [Fig. 2(b)] in the near field and at $x = 274$ mm [Fig. 2(c)] and $x = 549$ mm [Fig. 2(d)] in the far field. These wave fronts correspond to the phase isovalues of the acoustic pressure wave represented at the locations $0.36L_f$, $0.55L_f$, L_f, and $2L_f$, respectively. As the wavelength is very
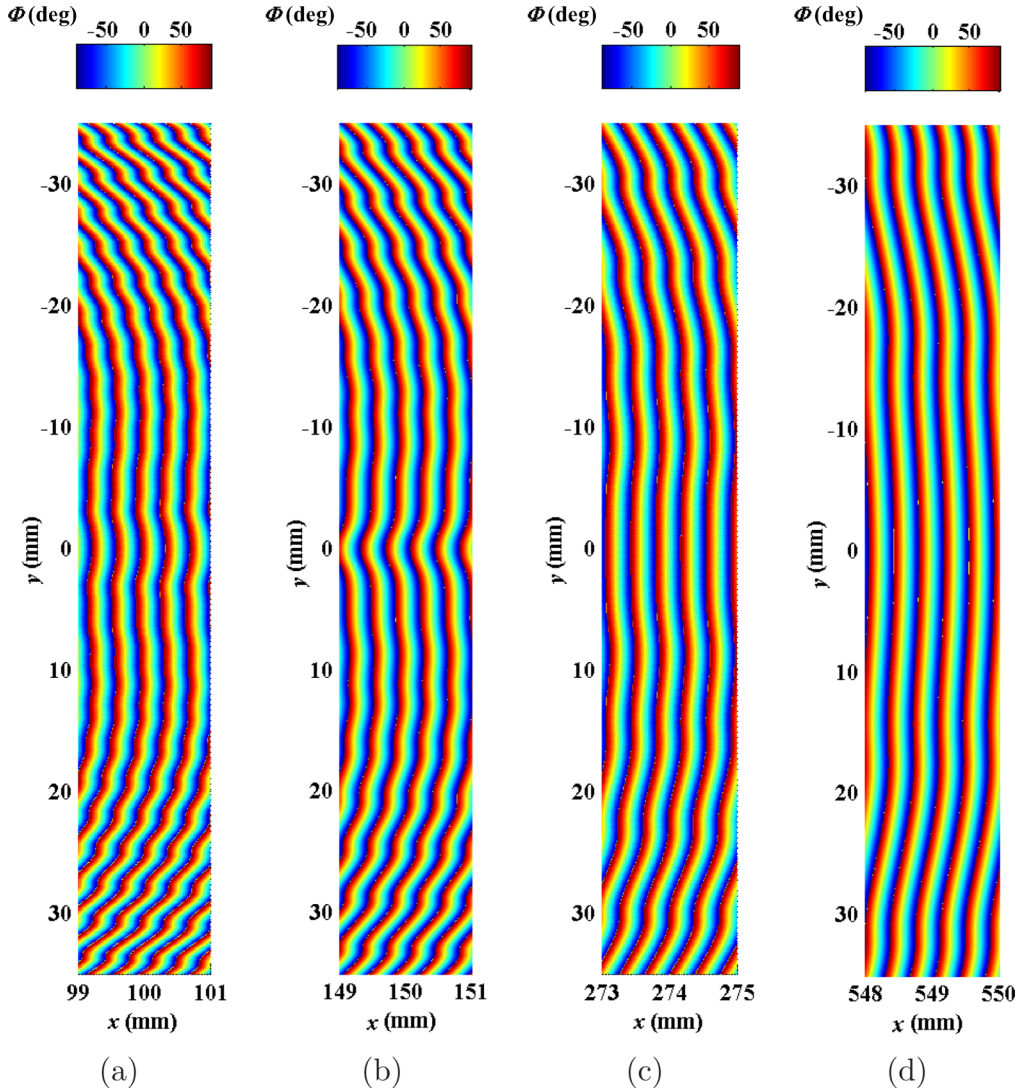
FIG. 2. (Color online) Plots of the phase isocontours of the acoustic wave in the near field at (a) $x = 100$ mm ($0.36\,L_f$) and (b) $x = 150$ mm ($0.55\,L_f$) and in the far field at (c) $x = 274$ mm (L_f) and (d) $x = 549$ mm ($2L_f$).

short ($\lambda = 0.74$ mm), the phase isocontours are represented in very thin areas (2 mm along x and 70 mm, namely more than two diameters, along y). In that way, the phase isovalues are depicted on almost three wavelengths and on a transverse length greater than the source diameter (notice that a wavelength corresponds to two color variations on the plot). We see that in both the near field and the far field the isovalues are not rigorously straight. In the central part (-20 mm $\leqslant y \leqslant$ $+20$ mm), however, the deviation along x for a given isovalue (measured, for example, between $y = 20$ mm and the center) is very short (a few tenths of millimeters) compared to the source diameter, so the wave front can be considered as a plane in this domain. Outside this domain ($y > +20$ mm or $y < -20$ mm), the isovalues have a stronger curvature, particularly in the near field, but the acoustic force intensities are much smaller in these zones. These observations thus support the validity of the plane-wave assumption, used to derive Eqs. (1) and (3), in the area of interest for our present purposes, that is, the region of the acoustic beam where the acoustic force is strong and where the hydrodynamic jet principally develops.

IV. COMPARISON OF EXPERIMENTAL AND NUMERICAL RESULTS

The experimental velocity fields measured for $P = 4$ W and the corresponding numerical velocity fields obtained for $f_{ac\ max} = 1.5\ \mathrm{N\,m^{-3}}$ are plotted in the xy horizontal plane in Figs. 3(a) and 3(b), respectively. A good agreement on the global flow structure can first be noted between the experimental measurements and the numerical calculations. As expected, the flow is characterized by a central jet with a very slow backflow on the sides of the fluid domain. A comparison with the velocity fields corresponding to the two other acoustic power values shows that the flow structure does not depend on the acoustic power in the investigated range ($2\,\mathrm{W} \leqslant P \leqslant 8\,\mathrm{W}$) [22]. A close look at the transverse velocity profiles in this vector plot allows us to see that they exhibit one or several local maxima, depending on the considered abscissa, as expected from Kamakura *et al.* [18].

Figure 4(a) shows the variations of the longitudinal velocity along the acoustic beam axis at $P = 2$, 4, and 8 W. As already mentioned, each profile has been measured in two separate PIV
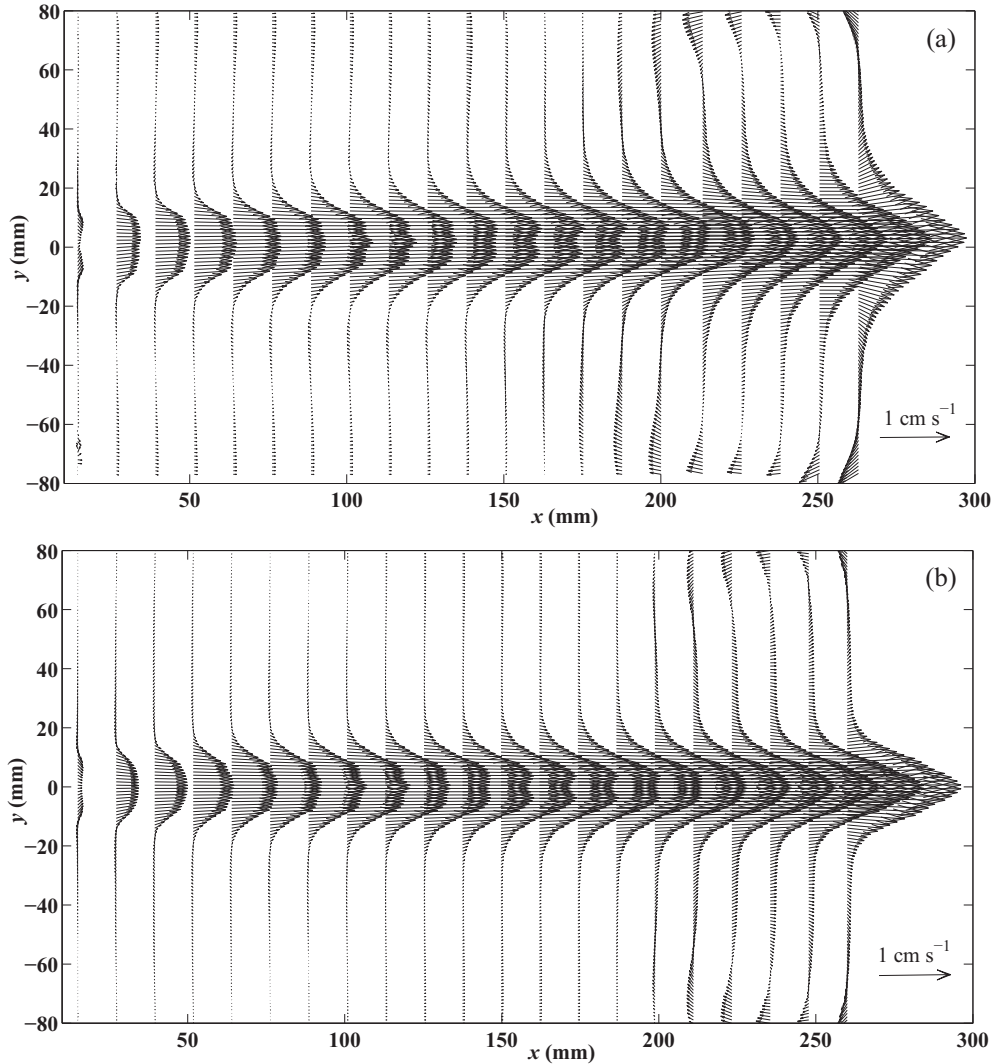
FIG. 3. Velocity vector maps in the xy horizontal plane including the acoustic beam axis. (a) Experimental measurements with the PIV technique for $P = 4$ W. (b) Numerical computations for $f_{ac\,max} = 1.5$ N m^{-3}. The velocity fields for the two other considered values of P can be found in Moudjed [22].

runs; between these two runs, the camera and the illuminating laser sheet had to be moved along the aquarium with the risk of modifying the alignment of the laser sheet with the acoustic beam axis. In spite of this, there is a good connection between the two parts of these profiles, as can be seen in Fig. 4(a). The profiles obtained numerically are also plotted with red dashed lines and a good agreement with the experimental profiles is observed. The axial velocity increases throughout the major part of the cavity and eventually drops suddenly to zero, as a consequence of the no-slip condition at the end wall. The initial curvature of the profiles, at small abscissa, is unexpectedly positive (increase of the slope) on a distance of a few millimeters [see the inset in Fig. 4(a)]. A wavering of the velocity profiles is also observed in a large part of the increasing portion. Note, finally, that electric powers of 2, 4, and 8 W yield maximum velocities of 1, 1.5, and 2.1 cm s^{-1}, respectively.

The numerical velocity profiles are then normalized and plotted with the normalized acoustic intensity profile in Fig. 4(b). This acoustic intensity profile along the acoustic beam axis is an exact analytic solution of Rayleigh's integral [23]. Note also that, in Fig. 4(b), the abscissa is scaled with the Fresnel length L_f. The local overvelocities and local undervelocities clearly correspond to the position of the acoustic intensity extrema. From the location of the last minimum of I_{ac} to the Fresnel length, the acoustic intensity increases; the axial velocity does as well, except close to the end wall. Note here again that the velocity profile shapes are very similar for the three considered values of electric power.

Figure 5 provides the normalized transverse velocity profiles obtained experimentally at $x = 50, 100, 150,$ and 200 mm from the transducer surface for the three considered powers. The normalized experimental acoustic intensity profiles at the same locations are also plotted as dashed lines, together with the normalized numerical velocity profiles obtained for $f_{ac\,max} = 1.5$ N m^{-3} plotted as solid lines. It can first be observed that, regardless of the acoustic power, the experimental velocity profile shapes are very similar, except
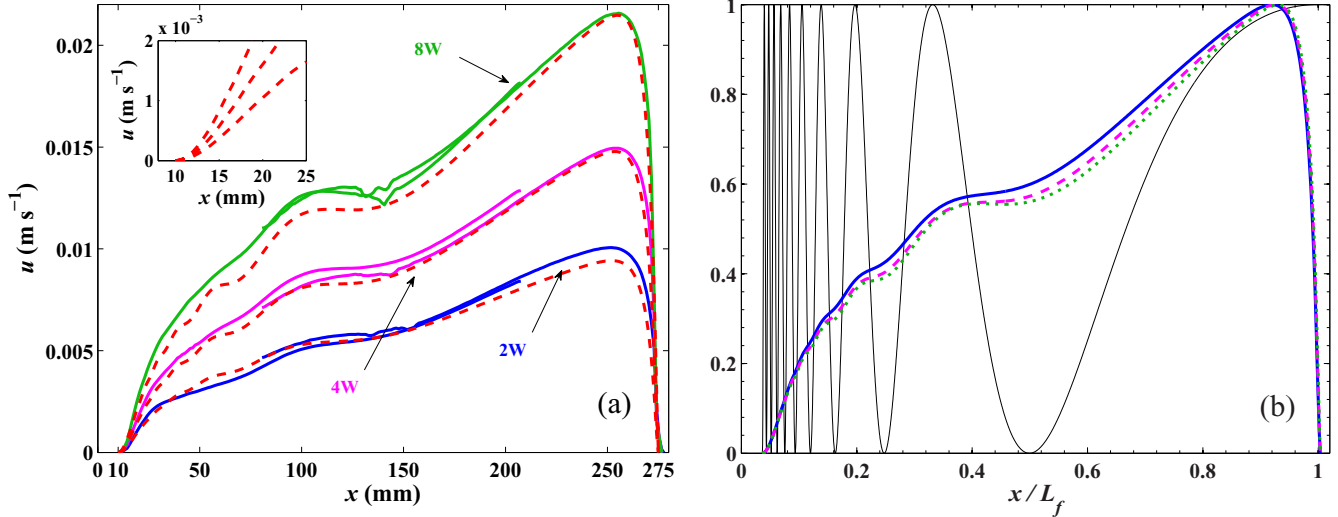
FIG. 4. (Color online) (a) Longitudinal profiles of the experimental axial velocity along the acoustic beam axis for $P = 2$ W (blue solid lines), 4 W (pink solid lines), and 8 W (green solid lines); the profiles obtained by the corresponding numerical calculations are also plotted as red dashed lines for $f_{ac\,max} = 0.725$, 1.5, and 2.9 N m^{-3}. These three numerical profiles are normalized and plotted in (b) with blue solid lines, pink dashed lines, and green dotted lines, respectively; the normalized acoustic intensity along the beam axis is also plotted as a black line (analytical expression [23]).

in the low-velocity backflow region. Such shapes are also reproduced by the normalized numerical velocity profiles. Moreover, a correlation can here again be noted between the shape of the acoustic intensity profiles and the shape of the velocity profiles. For instance, at $x = 100$ mm, the local peak in velocity corresponds to the acoustic intensity central peak. At $x = 150$ mm, the two local velocity maxima correspond to the two acoustic intensity peaks. Closer to the Fresnel length, as for $x = 200$ mm, acoustic and velocity profiles become smoother and closer in shape to those expected in the acoustic far field [17], whereas at a small distance from the transducer, as for $x = 50$ mm, the velocity profile does not follow the rapid spatial variations in acoustic intensity. Thus, though the correlation in shape between velocity profiles and acoustic intensity profiles is not perfect, we observe steady-state velocity profiles featuring several local maxima corresponding to local acoustic intensity maxima. To the best of our knowledge, such a feature has only been observed once before, by Kamakura *et al.* [18], but in a different situation, namely in the vicinity of the Fresnel length for transient (i.e., in the early stages of the jet, before steady state is reached) velocity profiles. In another context, the Fresnel diffraction in the near field is observed to promote fingering instabilities in a spreading film under surface acoustic waves [24].

Note that we only focus here on the jet part of the flow, which is the part that is forced by the acoustic wave. Due to the closed cavity configuration, the flow has to turn back at the end wall, and there is necessarily a backflow. This backflow, however, occurs in a vast area compared to the jet size and is then very slow: As a consequence of mass conservation, for a velocity of 2 cm s^{-1} in the central area of 3 cm in diameter, a fluid particle in the backflow region will take more than 8 min to cross the cavity length. A precise quantitative characterization of the flow in such a low-velocity region would need a specific experimental treatment, which is beyond the scope of the present paper.

V. SCALING ANALYSIS

Our objective in this section is to identify the leading mechanisms governing the main features of the fluid flow within the cavity. To this end, order of magnitude relations between the fluid velocity at a given axial location and other relevant quantities will be proposed. To start with, let us recall that in the zones of development of the acoustic streaming jet, a balance between inertia effects and the acoustic force can be expected [17]. This balance, in the case of a free acoustic streaming jet, can be written, on the beam axis, as

$$\rho u \frac{\partial u}{\partial x} \sim f_{ac} \qquad (4)$$

[u being a characteristic (e.g., the maximum) velocity at location x], which leads to the following scaling law:

$$u \sim \sqrt{\frac{f_{ac\,max}}{\rho} x'}, \qquad (5)$$

where $x' = x - x_0$ represents the distance to the upstream wall (Fig. 1). Note that a similar scaling has already been observed experimentally for the velocity in the acoustic far-field zone [17].

In Fig. 6, the velocities u calculated on the beam axis for the three values of $f_{ac\,max}$ are plotted as a function of the expression under the radical sign in Eq. (5). The simulation results obtained by Kamakura *et al.* [18] in the near field are also plotted. Let us recall that Kamakura's experiment featured a source with a different diameter and a different frequency ($d_s = 18$ mm, $f = 5$ MHz), so the plot of their data with ours is in itself a good test of the proposed scaling law; in particular, the attenuation coefficient in their experiment is expected to be 5.7 times larger. For each numerical velocity profile plotted in Fig. 6, a good agreement with the scaling law given by Eq. (5) (heavy black solid line) can be observed in an intermediate range of the abscissa values. In practice,
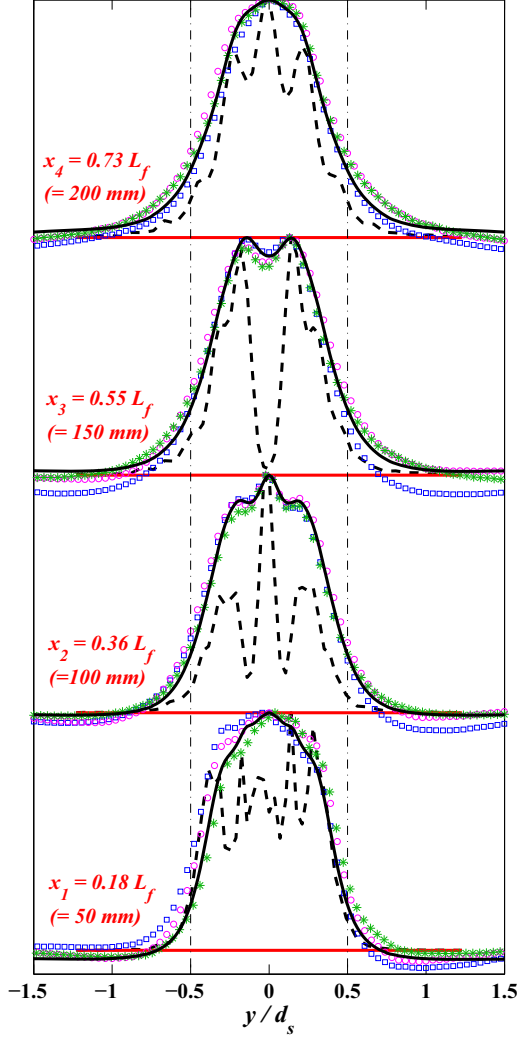
FIG. 5. (Color online) Horizontal transverse profiles of the normalized experimental acoustic intensity (black dashed lines), the normalized experimental velocity at $P = 2$ W (blue open squares), 4 W (pink open circles), and 8 W (green stars), and the normalized numerical velocity calculated with $f_{ac\,max} = 1.5$ N m^{-3} (black solid lines). These profiles are plotted at a distance $x = 50$, 100, 150, and 200 mm from the transducer. The black dotted-dashed vertical lines indicate the acoustic source diameter. Note that these plots are focused on the jet region, so the location of the lateral walls ($|y|/d_s \approx 3.2$) is not represented.
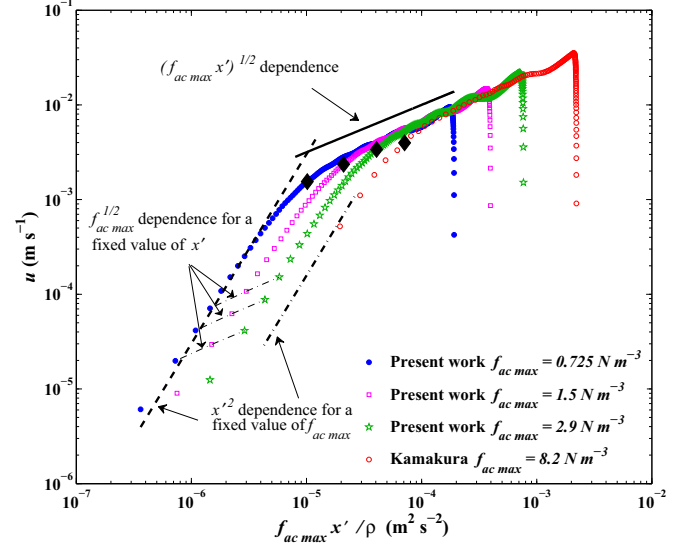

FIG. 6. (Color online) Longitudinal velocities along the acoustic beam axis plotted as a function of the expression appearing under the radical sign in Eq. (5). Four cases are presented corresponding to our simulations performed for $f_{ac\,max} = 0.725$, 1.5, and 2.9 N m^{-3} and the simulation of Kamakura *et al.* [18]. Two characteristic variations of the velocity are obtained: an initial quadratic increase, as depicted by the heavy black dashed line and heavy black dotted-dashed line obtained from Eq. (9) for $f_{ac\,max} = 0.725$ N m^{-3} and for Kamakura *et al.* [18], respectively, and a square-root increase, as depicted by the heavy black solid line obtained from Eq. (5). On the different numerical profiles, the black solid diamonds indicate the points located at the distance $d_s/2$ from the upstream wall, which give the transition between the two characteristic variations. The $f_{ac\,max}^{1/2}$ dependence in these different zones is also shown.

the square-root behavior is valid over the major part of the cavity. Of course, the scaling is not valid near the end wall due to the zero-velocity condition at the wall, which prevents the further increase of the velocity. More interestingly, the square-root scaling is also not observed near the upstream wall in a region where the velocity profiles have an intriguing initial positive curvature along x [i.e., an increase of the slope, see the inset in Fig. 4(a)]. In this region, typically 5 to 10 mm long in our experiments, the velocity is found to evolve approximately as x'^2 (Fig. 6). To assess this observation, mass conservation was applied in a thin cylindrical control volume close to the upstream wall, as depicted in Fig. 7. This mass budget involves an axisymmetric radial inflow and an axial

outflow. The characteristic radial velocity at $d_s/2$ (the radial limit of the transducer) can be written as

$$v_r \sim Sx', \qquad (6)$$

featuring a linear increase of the velocity in the boundary layer along the upstream wall. As depicted in Fig. 7(b), the axial velocity profiles close to the upstream wall can be considered as constant on a typical radial distance close to the acoustic source radius and almost zero outside this cylindrical domain, so the axial flow rate is simply $\pi d_s^2 u/4$. Concerning the radial flow rate, it is obtained by integrating (6) on the cylindrical surface of radius $d_s/2$ and height x'. Applying mass conservation, the axial velocity can thus be expressed as

$$u \sim 4\frac{Sx'^2}{d_s}, \qquad (7)$$

where S is still unknown. A further assumption, supported by the numerical simulations, is to suppose that the jet recirculates at the scale of the transducer radius [see Fig. 7(a)]. In other words, at $x' = d_s/2$, u given by Eq. (7) should match its far-field expression (5). Note that at this distance (represented by the black solid diamonds on the curves in Fig. 6), both our set of experiments and the experiment of Kamakura *et al.* [18] are well in a transition zone between the two observed scaling
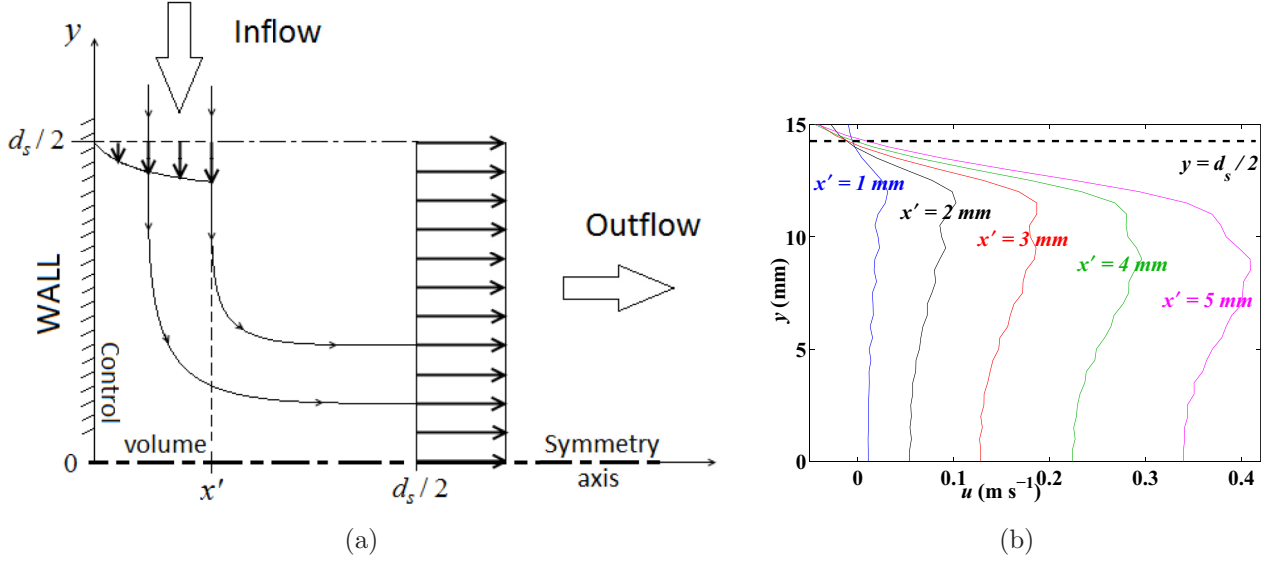
FIG. 7. (Color online) (a) Sketch showing a two-dimensional axisymmetric view of the region close to the upstream wall. Mass conservation is performed in a control volume between the inflow (radial velocity considered as linear in the boundary layer along the upstream wall) and the outflow (constant axial component for $0 \leqslant r \leqslant d_s/2$). Sketched streamlines are represented with black lines. (b) Radial profiles of the axial velocity obtained numerically for $f_{ac\,max} = 0.725$ N m^{-3} and given at different distances x' from the upstream wall.

laws. We thus get

$$S \sim \sqrt{\frac{f_{ac\,max}}{2\,\rho\,d_s}}. \tag{8}$$

Introducing this value of S in (7), we thus finally obtain

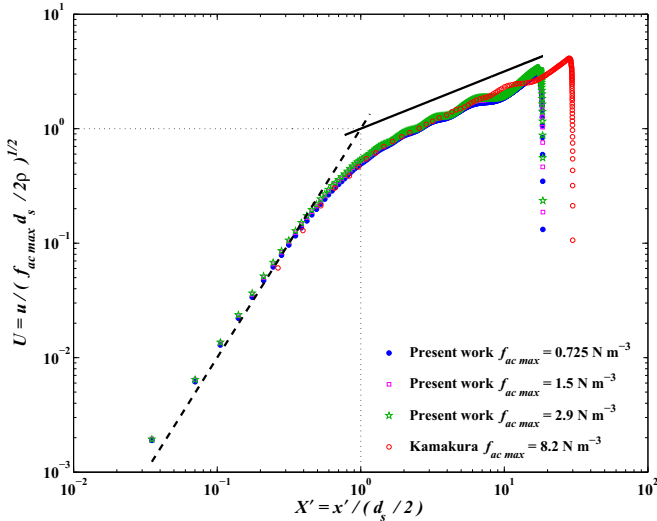$$u \sim 4 \sqrt{\frac{f_{ac\,max}}{2\rho}}\, d_s^{-3/2}\, x'^2. \tag{9}$$

FIG. 8. (Color online) Dimensionless longitudinal velocity $U = u/(f_{ac\,max}d_s/2\rho)^{1/2}$ along the acoustic beam axis plotted as a function of the dimensionless distance to the upstream wall $X' = x'/(d_s/2)$ for the different experiments. A collapse of the curves is observed and the two characteristic variations of the velocity are shown: $U = X'^2$ (heavy black dashed line) for $X' < 1$ and $U = X'^{1/2}$ (heavy black solid line) for $X' > 1$.

This expression of u is plotted in Fig. 6 as a heavy black dashed line for our situation at $f_{ac\,max} = 0.725$ N m^{-3} and as a black dotted-dashed line for the situation of Kamakura *et al.* [18] ($d_s = 18$ mm, $f_{ac\,max} = 8.2$ N m^{-3}). A good adjustment is found in both cases. Note also that a comparison between the values of u obtained in this zone at constant x' for different $f_{ac\,max}$ (see the thin black dotted-dashed lines in Fig. 6) indicates that u varies as $f_{ac\,max}^{1/2}$, as proposed in (9).

All these observations suggest that the typical scales for these experiments are the length scale $d_s/2$ and the value of u corresponding to the previous matching at $d_s/2$, i.e., $u = \sqrt{f_{ac\,max}d_s/2\,\rho}$ [obtained, for example, from (5)]. We then define new dimensionless variables, $X' = x'/(d_s/2)$ and $U = u/\sqrt{f_{ac\,max}d_s/2\rho}$. Note that U can be seen as a Froude number since it expresses the balance between inertia effects and a volumetric force [see Eqs. (4) and (5)]. As shown in Fig. 8, with this new scaling the different results corresponding to our simulations performed for $f_{ac\,max} = 0.725$, 1.5, and 2.9 N m^{-3} and the simulation of Kamakura *et al.* [18] collapse to a single curve (with a slightly different wavering for the two studied configurations), except close to the downstream walls located at the distances $X' = (x_L - x_0)/(d_s/2) = 18.6$ and 30 for our simulations and Kamakura's simulation, respectively. The two characteristic variations of the velocity are now given by $U = X'^2$ (heavy black dashed line) and $U = X'^{1/2}$ (heavy black solid line) which intersect at $X' = 1$.

VI. CONCLUSION

The objective of the present work was a numerical and experimental investigation of the acoustic streaming flow in the near field of a plane ultrasonic transducer in water. This study, in particular, gives spatially resolved experimental velocity profiles along the acoustic beam axis. A good agreement between the experimental measurements and the

numerical results for the velocity field is obtained. Despite the complex structure of the acoustic near field that exhibits spatial variations at very small scales, the plane-wave approach leading to expression (1) for the acoustic force can thus be taken as valid in this near-field zone, a result which is supported by the observed shape of the wave fronts in the region of high acoustic intensity corresponding to the jet area. The use of a linear acoustic propagation model is also found to be suitable to compute the acoustic field and deduce the acoustic streaming force in the investigated range of parameters. Such acoustic propagation model is thus far simpler and lighter than the KZK model used by Kamakura *et al.* [18]. With a smaller computational time, it leads to results of the same quality concerning the correspondence between simulated flows and experiments.

The strong correlation between the acoustic field shape and the flow structure is confirmed: the wavering observed on the longitudinal profiles of the velocity is linked to the variations in acoustic intensity on the beam axis, and the complex shape of the transverse velocity profiles is directly linked to acoustic intensity transverse variations. In particular, we observe steady-state transverse velocity profiles featuring several local extrema in correlation with those of the acoustic

intensity profiles. Finally, different scaling laws are observed for the variation of the velocity along the jet axis. A strong initial acceleration is observed close to the upstream wall; the velocity scales there as x'^2, as a consequence of mass conservation near the wall, with a flow recirculating on a length scale characteristic of the acoustic source. Farther downstream, the velocity scales as $x'^{1/2}$, as a consequence of the 1D balance between inertia and the acoustic forcing; this scaling is observed to be valid over the rest of the cavity, except at the approach of the downstream wall. In both cases, the velocity scales as the square root of the applied maximum acoustic force. Finally, with an appropriate scaling of the distance from the upstream wall x' and of the longitudinal velocity, the variation of the velocity along the jet axis for the different experiments in the near-field zone can be represented with a single curve, except close to the downstream wall.

ACKNOWLEDGMENTS

[1] M. Faraday, On a peculiar class of acoustical figures; and on certain forms assumed by groups of particules upon vibrating elastic surfaces, Phil. Trans. R. Soc. Lond. **121**, 299 (1831).

[2] C. M. Poindexter, P. J. Rusello, and E. A. Variano, Acoustic Doppler velocimeter-induced acoustic streaming and its implications for measurement, Exp. Fluids **50**, 1429 (2011).

[3] A. Pothérat, F. Rubiconi, Y. Charles, and V. Dousset, Direct and inverse pumping in flows with homogeneous and non-homogeneous swirl, Eur. Phys. J. E **36**, 94 (2013).

[4] L. Clarke, A. Edwards, and K. Pollard, Acoustic streaming in ovarian cysts, J. Ultrasound Med. **24**, 617 (2005).

[5] X. Shi, R. W. Martin, S. Vaezy, and L. A. Crum, Quantitative investigation of acoustic streaming in blood, J. Acoust. Soc. Am. **111**, 1110 (2002).

[6] M. C. Charrier-Mojtabi, A. Fontaine, and A. Mojtabi, Influence of acoustic streaming on thermo-diffusion in a binary mixture under microgravity, Int. J. Heat Mass Transf. **55**, 5992 (2012).

[7] V. Frenkel, R. Gurka, A. Liberzon, U. Shavit, and E. Kimmel, Preliminary investigations of ultrasound induced acoustic streaming using particle image velocimetry, Ultrasonics **39**, 153 (2001).

[8] H. Ben Hadid, W. Dridi, V. Botton, B. Moudjed, and D. Henry, Instabilities in the Rayleigh-Bénard-Eckart problem, Phys. Rev. E **86**, 016312 (2012).

[9] W. Dridi, D. Henry, and H. Ben Hadid, Influence of acoustic streaming on the stability of a laterally heated three-dimensional cavity, Phys. Rev. E **77**, 046311 (2008).

[10] W. Dridi, D. Henry, and H. Ben Hadid, Influence of acoustic streaming on the stability of melt flows in horizontal Bridgman configurations, J. Cryst. Growth **310**, 1546 (2008).

[11] M. C. Schenker, M. J. B. M. Pourquie, D. G. Eskin, and B. J. Boersma, PIV quantification of the flow induced by an ultrasonic horn and numerical modeling of the flow and related processing times, Ultrason. Sonochem. **20**, 502 (2013).

[12] R. Barnkob, P. Augustsson, T. Laurell, and H. Bruus, Acoustic radiation- and streaming-induced microparticle velocities determined by microparticle image velocimetry in an ultrasound symmetry plane, Phys. Rev. E **86**, 056307 (2012).

[13] P. Brunet, M. Baudoin, O. Bou Matar, and F. Zoueshtiagh, Droplet displacements and oscillations induced by ultrasonic surface acoustic waves: A quantitative study, Phys. Rev. E **81**, 036315 (2010).

[14] M. B. Dentry, L. Y. Yeo, and J. R. Friend, Frequency effects on the scale and behavior of acoustic streaming, Phys. Rev. E **89**, 013203 (2014).

[15] J. Lighthill, Acoustic streaming, J. Sound Vibr. **61**, 391 (1978).

[16] Wesley L. Nyborg, *Acoustic Streaming* (Academic Press, San Diego, CA, 1998).

[17] B. Moudjed, V. Botton, D. Henry, H. Ben Hadid, and J. P. Garandet, Scaling and dimensional analysis of acoustic streaming jets, Phys. Fluids **26**, 093602 (2014).

[18] T. Kamakura, T. Sudo, K. Matsuda, and Y. Kumamoto, Time evolution of acoustic streaming from a planar ultrasound source, J. Acoust. Soc. Am. **100**, 132 (1996).

[19] S. I. Aanonsen, T. Barkve, J. N. Tjotta, and S. Tjotta, Distortion and harmonic generation in the nearfield of a finite amplitude sound beam, J. Acoust Soc. Am. **75**, 749 (1984).

[20] V. P. Kuznetsov, Equations of nonlinear acoustics, Sov. Phys. Acoust. **16**, 467 (1971).

[21] C. E. Bradley, Acoustic streaming field structure: The influence of the radiator, J. Acoust. Soc. Am. **100**, 1399 (1996).

[22] B. Moudjed, PhD. thesis, INSA de Lyon, 2013.

[23] D. T. Blackstock, *Fundamentals of Physical Acoustics* (John Wiley & Sons, New York, 2000).

[24] A. R. Rezk, O. Manor, J. R. Friend, and L. Y. Yeo, Unique fingering instabilities and soliton-like wave propagation in thin acoustowetting films, Nat. Commun. **3**, 1167 (2012).